RSC Advances

This is an *Accepted Manuscript*, which has been through the Royal Society of Chemistry peer review process and has been accepted for publication.

Accepted Manuscripts are published online shortly after acceptance, before technical editing, formatting and proof reading. Using this free service, authors can make their results available to the community, in citable form, before we publish the edited article. This *Accepted Manuscript* will be replaced by the edited, formatted and paginated article as soon as this is available.

You can find more information about *Accepted Manuscripts* in the **Information for Authors**.

Journal Name

ARTICLE

Synthesis of Mo-doped WO₃ nanosheets with enhanced visible-light-driven photocatalytic properties

Naixu Li[a], Hongcheng Teng[a], Li Zhang[a], Jiancheng Zhou*[a,b], Maochang Liu*[c]

Ions doping provides a powerful means for the fabrication of a functionalized photocatalyst that is both active and stable. Herein, a series of Mo-doped monoclinic WO₃ photocatalysts, in the form of well-shaped 2-dimension (2D) rectangular nanosheets, were successfully synthesized via a simple hydrothermal process. It is assumed that Mo was homogeneously doped into the crystal lattice of WO₃. In addition to the 2D structure beneficial for charge transfer, Mo doping altered the band structure of WO₃, enabling the further improvement of photocatalytic activity on rhodamine B degradation over the nanosheets.

1. Introduction

Semiconductor mediated photocatalysis has become a promising technologies in wastewater treatment.[1-3] Among the semiconductor photocatalysts, TiO₂ is the most widely used photocatalyst because of its good stability, non-toxicity and excellent photocatalytic activity.[4,5] However, TiO₂ can only adsorb the ultraviolet light, which occupies a little part of solar light, due to its wide band gap (3.2 eV). Selecting novel visible-light-driven photocatalytic materials have been investigated because of their special band structure and efficient use of solar energy.

Tungsten oxide (WO₃) is an n-type semiconductor which has good thermal stability, photosensitivity, stability against photocorrcsion and good electron transport properties,[6,7] and has been extensively used infrared switching devices,[8] catalysis,[9,10] gas sensors,[11-13] photoelectrochemical systems[14-16] and flat panel.[17] Although WO₃ has these promising characteristics, the band gap of WO₃ (~2.8)[18-20] is still large to absorb sufficient solar spectrum. The photocatalytic performance of WO₃ could be improved by modification WO₃ through semiconductor coupling,[21-27] noble metal deposition[28],

[29] and doping,[30-36] etc.

Among them, doping is an effective strategy for narrowing the band gap of WO₃ and enhancing photocatalytic activities. Sun et al. doped carbon on WO₃, which decreased the band gap and enhanced photocurrent density of C-doped WO₃ electrode.[35] Song et al. synthesized Fe-doped WO₃ nanostructures and founded a greatly enhancement of visible light photocatalytic activity after doping Fe because of the red shift in the optical absorption of WO₃ and trapping effect.[32] Feng et al. reported that Ti doped WO₃ nanocuboids exhibit much better photoactivity than that of pure WO₃.[31] The ionic radius of molybdenum[37] is close to that of tungsten[38], which enables molybdenum to incorporate into the tungsten lattice and improve the photocatalytic properties of WO₃ in the visible range. Zhang et al. reported phase-pure Bi₂MoₓW₁₋ₓO₆ photocatalysts that could better utilize visible light after doing Mo.[39] Song et al. prepared a novel Mo-doped WO₃ nanowires exhibiting an excellent photocatalytic dye degradation.[33] However, underlining mechanism for various WO₃ based catalysts, especially Mo doing, remained unclear and held great potential for further exploitation.

Herein, we described a facile synthesis of Mo-doped WO₃ photocatalysts in the form of well-shaped 2-dimension (2D) rectangular nanosheet by an organic-additive-free hydrothermal method and their photocatalytic performances in the degradation of rhodamine B (RhB) under visible light irradiation. Furthermore, the roles of different reactive species were explored by introducing various scavengers into the photocatalytic reaction system. In addition, the possible mechanism of photocatalytic activity enhancement of Mo doped WO₃ nanosheets was proposed.

a School of Chemistry and Chemical Engineering, Southeast University, Nanjing, Jiangsu, 211189 (P. R. China), E-mail: jczhou@seu.edu.cn
b Department of Chemical and Pharmaceutical Engineering, Southeast University Chengxian College, Nanjing, Jiangsu, 210088 (P.R. China), E-mail: jczhou@seu.edu.cn
c International Research Center for Renewable Energy, State Key Laboratory of Multiphase Flow, Xi'an Jiaotong University, Xi'an, Shaanxi 710049 (P. R. China), E-mail: maochangliu@mail.xjtu.edu.cn

RSC Advances Accepted Manuscript

2. Experimental Section

2.1 Chemicals and materials

Sodium tungstate dehydrate ($Na_2WO_4 \cdot 2H_2O$), hexaammonium heptamolybdate tetrahydrate (($NH_4)_6MoO_{24} \cdot 2H_2O$), sodium hydroxide (NaOH), nitric acid(HNO_3), hydrochloric acid (HCl) and rhodamine B (RhB) were all purchased from the Shanghai Chemical Reagent Company in analytical grade, and were used as received without further purification. Deionized water was used throughout the whole experiment.

2.2 Synthesis of the Mo doped WO_3 materials

Mo doped WO_3 nanosheets were successfully synthesized according to a simple hydrothermal method.[10] Typically, 10 mL of 65% nitric acid was dissolved in distilled water(40 mL) and stirred for 10 min.1 g $Na_2WO_4 \cdot 2H_2O$ and a certain amount of $(NH_4)_6MoO_{24} \cdot 2H_2O$ were dissolved homogeneously in 20 mL distilled water and were slowly added into the above solution under continuous magnetic stirring. After stirring for another 30min, the above suspension was transferred into a 100 ml Teflon-lined stainless-steel autoclave, sealed and heated to 180 ^{o}C for 3h. After cooling naturally, the product was centrifuged and washed with distilled water and ethanol several times. The sample was dried in vacuum at 60 ^{o}C for 12 h. The prepared samples with 0.5, 1, 2, 5, 10% Mo, defined as the molar ration of Mo to WO_3, were named as S1, S2, S3, S4, S5.

2.3 Characterization

The structural and morphology of the samples were characterized by X-ray diffraction (XRD, Bruker D8-Discover with Cu-Kα radiation), Scanning electron microscopy (SEM, JSM-7800F), transmission electron microscopy (TEM, Hitachi H-600, FEI Tecnai G2 F30) and X-ray photoelectron spectroscopy (XPS, 2000 XPS system with a monochromatic Al-Ka source). Diffuse reflectance UV-visible spectra of the samples were obtained from a Shimadzu UV 3600 spectrometer. The BET surface areas of the samples were obtained from a Micromeritics ASAP 2020M system at liquid nitrogen temperature (77K). The chemical composition of the samples was analysed by inductively coupled plasma optical emission spectrometer (ICP-OES, Varian ICP-OES 720). The zeta potentials of the samples in aqueous suspension were measured as a function of pH using a Zetasizer Nano ZS 90 (Malvern).

2.4 Photocatalytic activity testing

The photocatalytic activities of the samples were evaluated through the photocatalytic degradation of rhodamine B (RhB) in aqueous solution under visible light from a 500W Xe lamp furnished with a 420 nm cutoff filter at room temperature. Typically, 0.20 g of photocatalyst was dispersed in 200mL of 30 mg L^{-1} aqueous RhB solution. Before the light was turned on, the suspensions were magnetically stirred for 30 min in the dark to establish an adsorption-desorption equilibrium. 5 mL of the sample was extracted in a 30 min interval. The absorbance of RhB was measured by a 722s spectrophotometer (Shanghai Precision and Scientific Instrument Company, China) with the

maximum absorption wavelength at 554nm. The photocatalytic performance was measured by the dye removal rate, which is calculated by the following formula:

$$D = \frac{C_0 - C}{C_0} \times 100\%$$

where D (%) is the degradation rate, C_0 (mg L^{-1}) denotes the initial RhB concentration, and C (mg L^{-1}) represents the RhB concentration in the filtrates after irradiation.

3. Results and discussion
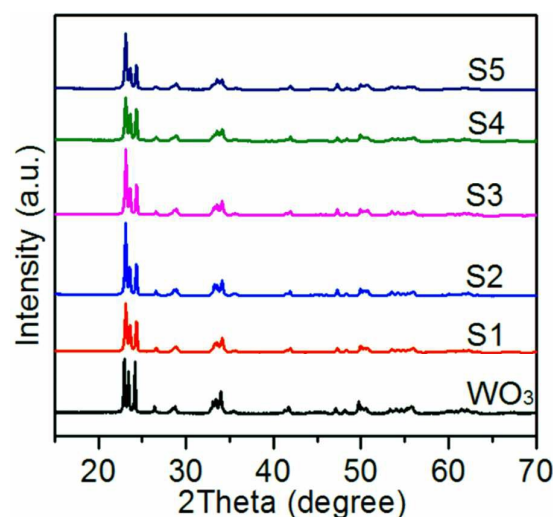
Fig. 1 XRD patterns of WO_3, S1, S2, S3, S4, S5.

Fig.1 shows the XRD patterns of the as-prepared of WO_3 and Mo doped WO_3 nanosheets synthesized by hydrothermal method. The pure WO_3 could be well indexed to the monoclinic WO_3 (JCPDS 43-1035) with the lattice constants of a = 0.7297 nm, b = 0.7539 nm, c = 0.7688 nm, and β = 90.91°. With the increasing Mo contents, no apparent peaks of molybdenum trioxide or other phases could be detected in the doped samples. This phenomenon could be attributed to the relatively low concentration of Mo and nearly the same radius of Mo^{6+} (0.59 Å) and W^{6+} (0.60 Å). In this case, Mo^{6+} ions were expected to homogeneously embed into the crystal lattice of WO_3 without affecting the crystal structures.

The morphology of these samples was then investigated by SEM. As shown in Fig. 2, all the samples possessed a rectangular sheet-like shape with the side length ranging from 400 to 1600 nm and a thickness round 150 nm. Similarly, the morphology of the samples was not changed with the increasing of Mo contents. The crystal structure was further examined by TEM, corresponding SAED patterns and HRTEM. As shown in Fig. 3(a), the rectangular structure was further confirmed by the 90° corner of a crystal. The SAED pattern (Fig. 3c) indicates that the WO_3 nanosheets were single-crystalline. An interplanar spacing of 0.382 nm as shown in Fig. 3e can be indexed to the 002 lattice diffraction of WO_3. Again, with the same reason mentioned above, no notable

RSC Advances

lattice space changes can be observed after doping 1% Mo (Fig. 3d-f). To further confirm the existence of Mo in WO_3 nanosheets, the doped WO_3 was characterized by STEM-EDX mapping. Obviously, as shown in Fig. 4, homogeneous distributions of W and O were observed in the nanosheets (Fig. 4b–c) which were consistent to the SEM image. Highly dispersed Mo element with quite low density could also be observed (Fig. 4d).

Table 1 Physicochemical properties and photocatalytic performances of as-prepared samples.

Sample	Theoretical Mo content (at. %)	Average Mo content (at. %)[a]	surface Mo content (at. %)[b]	Surface area (m^2/g)[c]	Band gap (eV)	Zeta potential (mV at pH 12)	Degradation rate (%)
WO_3	0	0.00	0	7.852	2.60	-34.3	59.3
S1	0.5	0.49	0.38	9.884	2.56	-34.1	70.0
S2	1	0.94	0.67	8.103	2.51	-36.7	92.8
S3	2	1.97	1.43	8.274	2.46	-37.2	64.5
S4	5	4.75	3.43	8.683	2.39	-37.9	36.2
S5	10	9.97	8.37	8.425	2.36	-39.4	30.1

[a] Mo content measured ICP-OES. [b] Mo content measured from XPS. [c] BET surface area.
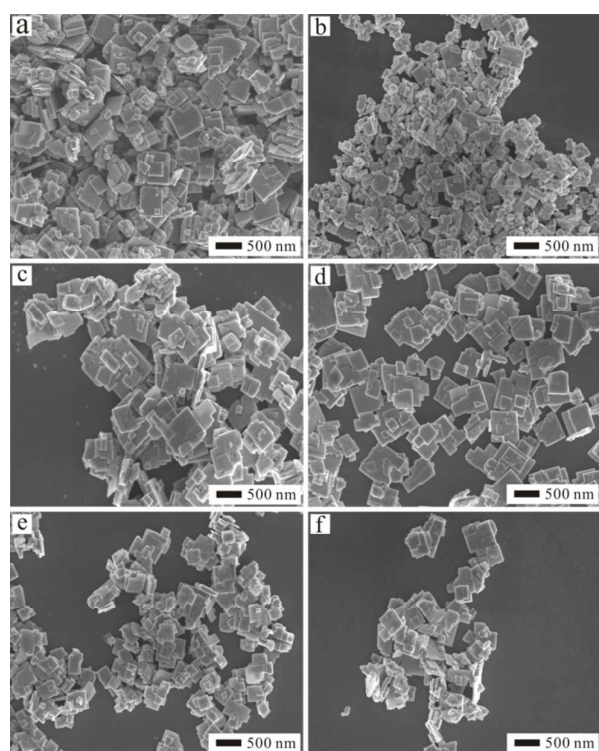
Fig. 2 (a), (b), (c), (d), (e) and (f) are the SEM images of the as-prepared WO_3, S1, S2, S3, S4 and S5, respectively.
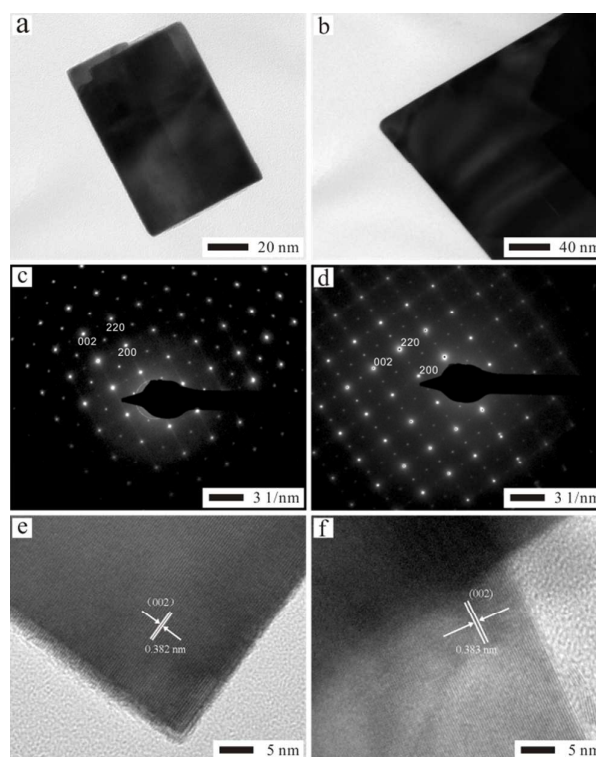
Fig. 3 (a), (c), (e) are TEM, corresponding SAED patterns and HRTEM images of WO_3; (b), (d) and (f) are TEM, corresponding SAED patterns and HRTEM images of S2.
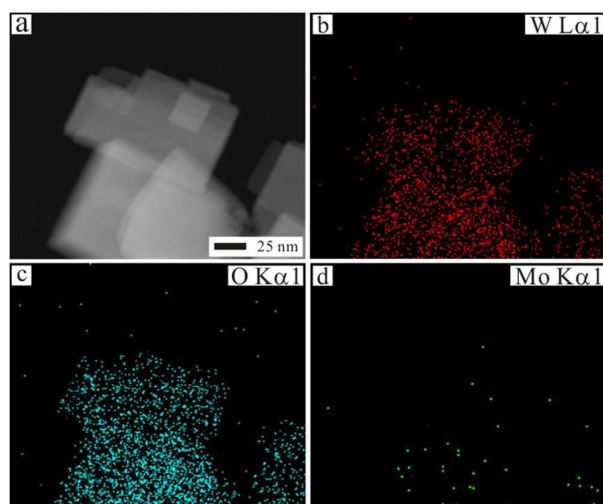
Fig. 4 (a) STEM image of S2 and (b-d) the corresponding EDX mapping of S2 at the region shown in (a) , indicating spatial distribution of W, O, Mo, respectively.

The BET surface areas of the samples were carried out at liquid nitrogen temperature (77K), and the corresponding values were listed in Table 1. As can be seen, the pure WO_3 displays a lowest BET surface area 7.852 m^2/g. the surface areas Mo doped WO_3 nanosheets were between 8.103 to 9.884 m^2/g. These results implied that the BET surface areas of the samples are not changed significantly.
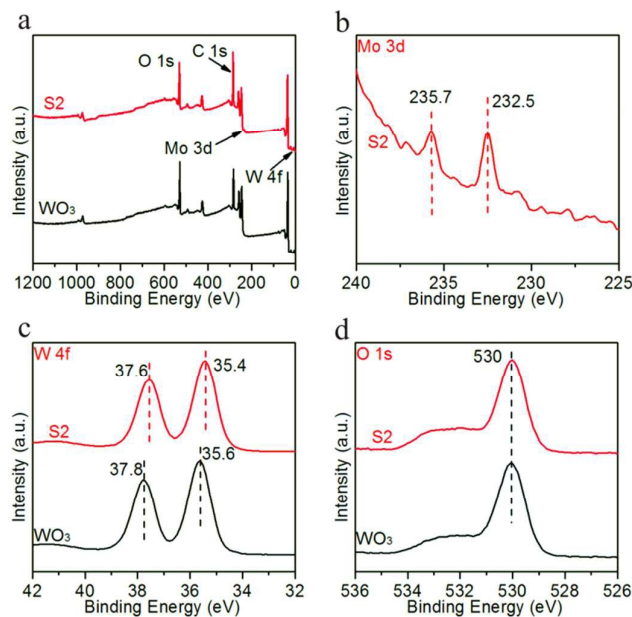
Fig. 5 (a) XPS survey spectra of sample WO_3 and S2, (b-d) high resolution XPS spectra of Mo, W and O.

We then investigated the surface chemical compositions and electronic structure of the as-prepared samples by X-ray photoelectron spectroscopy (XPS) analysis. As shown in Table

1, the surface Mo content was similar to the bulk chemical composition measured by ICP-OES, indicating a homogeneous distribution of Mo in the as-prepared samples. Fig. 5a presented the comparison of survey spectra of WO_3 and 1% Mo doped WO_3. Clearly, except Mo, both samples have shown binding energies originated from W, O, and C. The appearance of C peaks could attribute to adventitious carbon from the air. A close examination using high resolution XPS scan was then carried out on Mo 3d, W 4f and O 1s (Fig. 5b-d). Two peaks in Fig. 5b at 235.7 and 232.5 eV could be assigned to Mo 3d3/2 and 3d5/2, respectively, suggesting the Mo (VI) state in the samples.[40] Significantly, the binding energy of W 4f in the doped sample reduced by 0.2 eV. The shift could be owed to the substitution of Mo^{6+} for W^{6+} in the monoclinic lattice and thereby the formation of W-O-Mo bonds.[41]
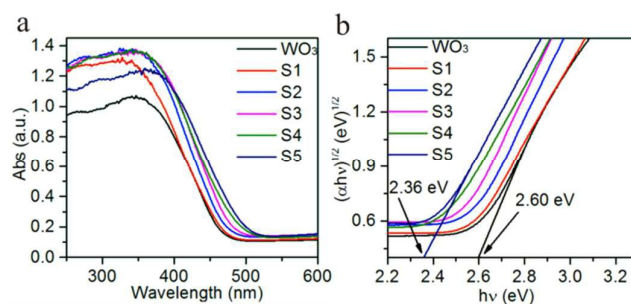
Fig. 6 (a) UV-vis absorption spectra of WO_3 and Mo-doped WO_3 nanosheets, (b) Plots of $(\alpha h\upsilon)^2$ versus photon energy (hυ) for the band gap energies of WO_3 and Mo-doped WO_3 nanosheets.

Optical property is one of the most important factors to evaluate the light utilization efficiency of a given photocatalyst. To this end, the as-prepared samples were further investigated by UV-vis spectra. As shown in Fig. 6a, all samples showed single steep edges, with onsets gradually shifted from 460nm to 540 nm when the doping amount of Mo was increased, indicating a band-gap based transition. The band gap of the samples could be calculated according to the following formula[42]:

$$\alpha h\upsilon = A(h\upsilon - E_g)^{n/2} \tag{1}$$

Where α, υ, E_g and A are absorption coefficient, light frequency, band gap energy, and a constant, respectively. Among them, n depends on the type of optical transition of a semiconductor (n=1 for direct transition and n=4 for indirect transition). For WO_3, the value of n is 4 for the indirect transition.[43] According to Eq. (1), the energy of band gap (E_g) can be estimated from a plot of $(\alpha h\upsilon)^{1/2}$ versus energy (hυ), while its value can be obtained by the intercept of the tangent to the X axis (Fig. 6b). E_g of WO_3 was calculated to be 2.60 eV. And E_g of Mo doped WO_3 decreased from 2.56 to 2.36 eV with the increase of Mo atom content from 0.5 to 10%, as shown in Tabe 1. This decrement should be a result from the narrowed band levels composited by Mo, W and O orbits.

The valence band (VB) edge position of Mo doped WO_3 nanosheets was estimated according to the concepts of electronegativity. Herein, the electronegativity of an atom is the

arithmetic mean of the atomic electron affinity and the first ionization energy. The valence band (VB) edge potential of a semiconductor at the point of zero charge can be calculated by flowing empirical equation[44-46]:

$$E_{VB} = X - E^C + 0.5E_g$$

where E_{VB} is the VB edge potential, X is the electronegativity of the semiconductor, which is the geometric mean of the electronegativity of the constituent atoms, E^C is the energy of free electrons on the hydrogen scale (about 4.5eV), E_g is the band gap energy of the semiconductor. The conduction band (CB) edge potential (E_{CB}) can be determined by $E_{CB} = E_{VB} - E_g$. The X value for WO_3 is ca. 6.68, and the E_{VB} of WO_3 is calculated to be 3.48 eV. Thus, the E_{CB} of WO_3 is estimated to be 0.88 eV.
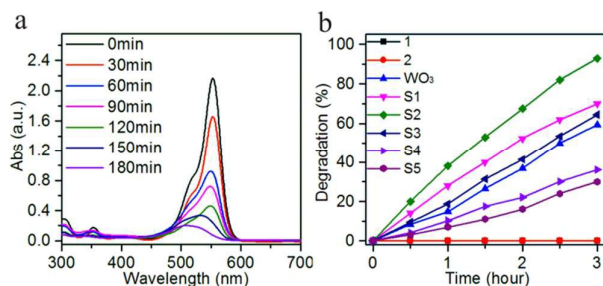
Fig. 7 (a) UV-vis absorption of RhB with variation of irradiation time over S2 at pH 12, (b) photodegradation of RhB at pH 12 under visible light under the same conditions with different photocatalysts (line 1: without any photocatalyst; line 2: with S2 without light)

The photocatalytic activity of the Mo doped WO_3 nanosheets was evaluated by degrading an aqueous solution of RhB at pH 12. Fig. 7a displays a gradual decrease of RhB absorption at the wavelength of 554nm under visible light irradiation. The comparison of activities for samples with different contents of Mo was shown in Fig. 7b. Blank experiments without any catalyst indicated no degradation, which implied the photolysis process has a negligible contribution to the degradation process of RhB. With the catalyst without light, RhB was also not degraded. It could be observed that the photodegradation of RhB over pure WO_3 was merely 60% after 3 h of visible light irradiation. When Mo was introduced, the photoactivity was significantly improved. The degradation rate increased with the increment of the content of Mo and reached a peak value 92% at the doping amount of 1% Mo. The degradation rates of the samples were respectively shown in Table 1.
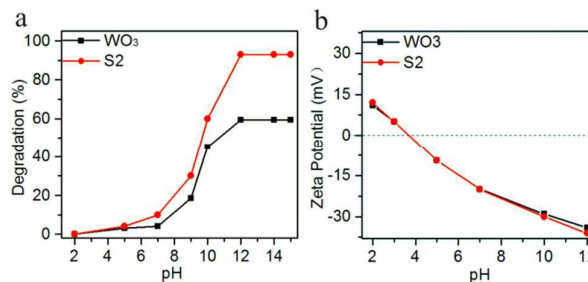
Fig. 8 (a) pH effect on the photodegradation of RhB with pure WO_3 nanosheets and S2 under visible light illumination for 3 h, (b) zeta potential of S2 suspended in water as a function of pH.

The reaction was also impacted by pH value of the suspension. Fig. 8a shows the photodegradation efficiency of RhB solution as a function of pH over WO_3 and 1% Mo-doped WO_3 photocatalysts. It could be found that the photodegradation efficiency in alkaline solutions was higher than that in acidic solutions. We further investigated the surface charge of WO_3 and 1% Mo-doped WO_3 photocatalysts by measuring the zeta potentials of suspended particles as a function of pH (Fig. 8b). No notable difference of the zeta-potential can be found between WO_3 and the doped one. Both samples show a zero charge at the pH value of around 4, which confirms the negative surface charge at high pH of WO_3. Under acidic conditions at pH value less than the points of zero charge, the positively charged WO_3 nanosheets may repel the cationic RhB group, reducing the dye adsorption and slowing degradation. Under alkaline conditions, the surface of WO_3 nanosheets is negatively charged and more readily adsorbs the RhB, promoting degradation. In addition the generating of hydroxyl radicals can be enhanced by the interaction between photogenerated holes and hydroxide ions (OH^-), which in turn would facilitate the photodegradation of RhB. Nevertheless, the photodegradation efficiency stopped increasing with pH values higher than 12. Similar arguments can be applied over the 1% Mo-doped WO_3 photocatalyst.
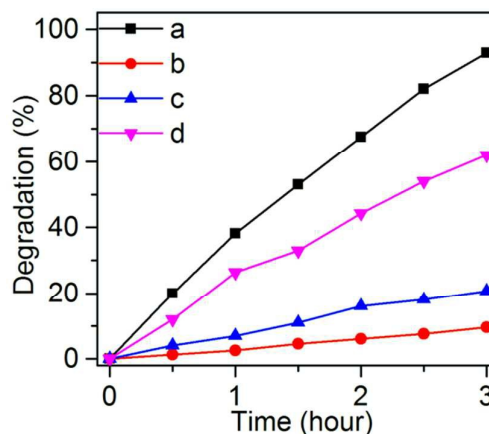
Fig. 9 Photodegradation of RhB using different radical scavenger and under N_2-saturated condition over 1% Mo-doped WO_3 nanosheets at pH

12: (a) no scavenger under O_2-saturated condition, (b) isopropanol for ·OH under O_2-saturated condition, (c) triethanolamine for h^+ under O_2-saturated condition, (d) no scavenger under N_2-saturated condition

To understanding the photocatalytic oxidation mechanism of RhB, radicals and holes trapping experiments were conducted. Fig. 9 displays the results of adding different scavengers into reaction system using the 1% Mo-doped WO_3 nanosheets as photocatalyst under visible-light irradiation. The photodegradation was significantly inhibited when a ·OH scavenger, namely isopropanol[47, 48] (Fig. 9b), was added. Obviously, the addition of isopropanol in the reaction system leaded to 80% decrease to the phtocatalytic degradation rate of RhB. A Similar inhibition phenomenon for the photocatalytic reaction was also observed with the presence of triethanolamine[49-51] scavenger for h^+ (Fig. 9c). Therefore, it could be concluded that ·OH and h^+ are the main reactive species for the degradation of RhB. The photodegradation decreased under the anoxic suspension (N_2-saturated condition, Fig. 9d), indicating that O_2 reacted with excited electrons to produce ·OH radicals.[10]

In a dye photosensitization process, the light irradiation excites electrons from the dye, and then the electrons can transfer to the conduction band of the catalyst and react with O_2 to generate the •O^{2-} oxidant[52]. The maximum RhB absorption band is located at 554 nm, so the energy provided by the Xe lamp is enough for the photosensitization of the dye. However, the main reactive species was ·OH, which implies that the photosensitization process is not the predominant process. It is well known that a dye photosensitization mechanism is closely related to the basic characteristics of the dye, such as the structural stability of the dye, the adsorbability of the dye on catalyst surface, and the absorbance of the dye under solar irradiation. WO_3 and Mo doped WO_3 nanosheets possessed similar surface areas (Table 1). The adsorbabilities of RhB thus are almost the same. Accordingly, it is suggested that the decrease of RhB concentration in the Mo doped WO_3 nanosheets system under visible light irradiation is initiated mostly by a photocatalytic process.
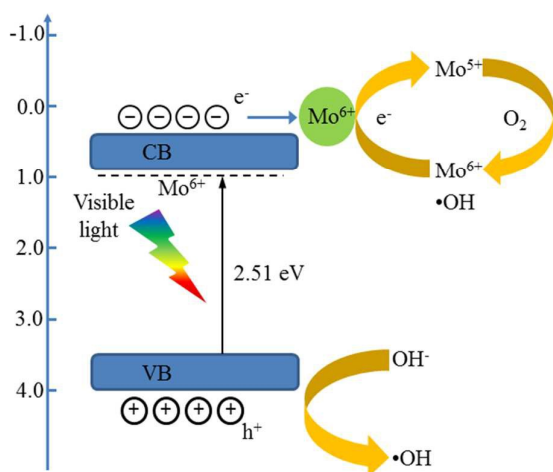
Fig. 10 The possible mechanism of the charge separation and the photocatalytic activity for the Mo doped WO_3 photocatalyst.

On the basis of above results, the possible photocatalytic process was summarized in Fig. 10. Firstly, doping Mo^{6+} ions could create a donor level under the conduction band of WO_3 to increase the absorption intensity of visible light.[39, 53] The valence bands of all samples were barely unchanged. The E_g of S2 is 2.51eV. The E_{VB} of S2 is 3.48 eV. Thus, the E_{CB} of S2 is estimated to be 0.97 eV. Therefore, more electrons could be excited under visible light region. Secondly, Mo^{6+} doped into the lattice of WO_3 could trap electrons to suppress recombination between electrons and holes.[54] The synergy between the two effects guaranteed the efficient enhanced photocatalytic activity towards RhB degradation over the doped WO_3 photocatalyst. The detailed reaction steps were showed as follows:

$$WO_3 + h\nu \rightarrow e^- + h^+ \tag{1}$$
$$h^+ + OH^- \rightarrow \bullet OH \tag{2}$$
$$Mo^{6+} + e^- \rightarrow Mo^{5+} \tag{3}$$
$$Mo^{5+} + O_2 + H_2O \rightarrow Mo^{6+} + \bullet OH \tag{4}$$
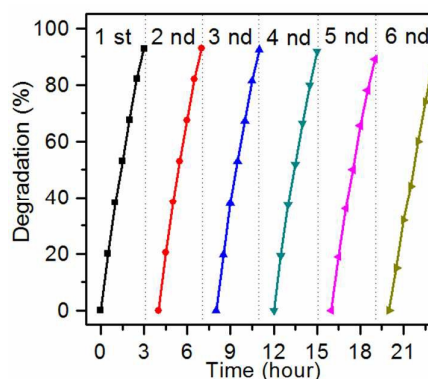
Fig. 11 Recyclability of photodegradation of RhB over S2 under visible-light irradiation for 180 min at pH 12.

The stability and reusability of photocatalysts are important factors for its application. Herein, we further investigated the stability of the 1% Mo doped WO_3 nanosheets. After six recycles for the photodegradation of RhB, no significant loss in photocatalytic activity is observed, as shown in Fig. 11, indicating an excellent stability of the Mo doped WO_3 nanosheets.

4. Conclusions

In summary, a series of Mo-doped WO_3 rectangular nanosheets were synthesized for the first time through a hydrothermal synthetic method. The Mo-doped WO_3 nanosheets exhibited enhanced photocatalytic activity compared to pure WO_3 nanosheets over the degradation of RhB under visible light irradiation. This improvement relied on the synergy of the well narrowed band gap of WO_3 and facilitated separation of the

photo-excited electrons and holes, both of which were created by Mo doping. The photocatalytic degradation of RhB was most efficient in alkaline conditions at pH 12. This work provides a facile way to synthesize different photocatalysts for enhancement visible-light-driven photocatalytic performance.

Notes and references

1. M. Basu, N. Garg and A. K. Ganguli, *J. Mater. Chem. A*, 2014, **2**, 7517-7527.
2. M. Mecklenburg, A. Schuchardt, Y. K. Mishra, S. Kaps, R. Adelung, A. Lotnyk, L. Kienle and K. Schulte, *Adv. Mater.*, 2012, **24**, 3486-3490.
3. C. P. Li, J. Q. Wang, S. Q. Feng, Z. L. Yang and S. J. Ding, *J. Mater. Chem. A*, 2013, **1**, 8045-8054.
4. A. Wold, *Chem. Mater.* , 1993, **5**, 280-283.
5. A. L. Linsebigler, G. Q. Lu and J. T. Yates, *Chem. Rev.*, 1995, **95**, 735-758.
6. J. Cao, B. Luo, H. Lin, B. Xu and S. Chen, *Appl. Catal., B*, 2012, **111-112**, 288-296.
7. Y. Peng, C. Liu, X. Zhang and J. Li, *Appl. Catal., B*, 2013, **140-141**, 276-282.
8. E. B. Franke, C. L. Trimble, J. S. Hale, M. Schubert and J. A. Woollam, *J. Appl. Phys.*, 2000, **88**, 5777-5784.
9. H. Habazaki, *Electrochim. Acta*, 2002, **47**, 4181-4188.
10. G. Zhang, W. Guan, H. Shen, X. Zhang, W. Fan, C. Lu, H. Bai, L. Xiao, W. Gu and W. Shi, *Ind. Eng. Chem. Res.*, 2014, **53**, 5443-5450.
11. X. Bai, H. Ji, P. Gao, Y. Zhang and X. Sun, *Sens. Actuators, B*, 2014, **193**, 100-106.
12. Z. Wang, P. Sun, T. Yang, Y. Gao, X. Li, G. Lu and Y. Du, *Sens. Actuators, B*, 2013, **186**, 734-740.
13. N. M. Vuong, H. Jung, D. Kim, H. Kim and S. K. Hong, *J.Mater. Chem.*, 2012, **22**, 6716-6725.
14. I. M. Szilágyi, B. Fórizs, O. Rosseler, Á. Szegedi, P. Németh, P. Király, G. Tárkányi, B. Vajna, K. Varga-Josepovits, K. László, A. L. Tóth, P. Baranyai and M. Leskelä, *J. Catal.*, 2012, **294**, 119-127.
15. X. H. Zhang, X. H. Lu, Y. Q. Shen, J. B. Han, L. Y. Yuan, L. Gong, Z. Xu, X. D. Bai, M. Wei, Y. X. Tong, Y. H. Gao, J. Chen, J. Zhou and Z. L. Wang, *Chem. Commun.*, 2011, **47**, 5804-5806.
16. D. S. Martínez, A. Martínez-de la Cruz and E. L. Cuéllar, *Appl. Catal., A*, 2011, **398**, 179-186.
17. M. Gratzel, *Nature*, 2001, **409**, 575-576.
18. A. Kudo and Y. Miseki, *Chem. Soc. Rev.*, 2009, **38**, 253-278.
19. H. L. Zhang, J. Q. Yang, D. Li, W. Guo, Q. Qin, L. J. Zhu and W. J. Zheng, *Appl. Surf. Sci.*, 2014, **305**, 274-280.
20. S. G. Kumar and K. S. R. K. Rao, *Appl. Surf. Sci.*, 2015, **355**, 939-958.
21. K. Lv, J. Li, X. Qing, W. Li and Q. Chen, *J. Hazard. Mater.*, 2011, **189**, 329-335.
22. C. C. Hu, J. N. Nian and H. Teng, *Sol. Energy Mater. Sol. Cells*, 2008, **92**, 1071-1076.
23. T. Arai, M. Horiguchi, M. Yanagida, T. Gunji, H. Sugihara and K. Sayama, *J. Phys. Chem. C*, 2009, **113**, 6602-6609.
24. J. Cao, B. Luo, H. Lin and S. Chen, *J. Hazard. Mater.*, 2011, **190**, 700-706.
25. S. J. Hong, S. Lee, J. S. Jang and J. S. Lee, *Energy Environ. Sci.*, 2011, **4**, 1781.
26. Z. F. Liu, Z. G. Zhao and M. Miyauchi, *J. Phys. Chem. C*, 2009, **113**, 17132-17137.
27. T. Huang, X. Lin, J. Xing, W. Wang, Z. Shan and F. Huang, *Mater. Sci. Eng., B*, 2007, **141**, 49-54.
28. Z. G. Zhao and M. Miyauchi, *Angew. Chem., Int. Ed. Engl.*, 2008, **47**, 7051-7055.
29. J. Kim, C. W. Lee and W. Choi, *Environ. Sci. Technol.* , 2010, **44**, 6849-6854.
30. W. J. Mu, X. Xie, X. L. Li, R. Zhang, Q. H. Yu, K. Lv, H. Y. Wei and Y. Jian, *Rsc Adv.*, 2014, **4**, 36064-36070.
31. C. Feng, S. Wang and B. Geng, *Nanoscale*, 2011, **3**, 3695-3699.
32. H. Song, Y. Li, Z. Lou, M. Xiao, L. Hu, Z. Ye and L. Zhu, *Appl. Catal., B*, 2015, **166-167**, 112-120.
33. X. C. Song, E. Yang, G. Liu, Y. Zhang, Z. S. Liu, H. F. Chen and Y. Wang, *J. Nanopart. Res.*, 2010, **12**, 2813-2819.
34. Y. Liu, Y. Li, W. Li, S. Han and C. Liu, *Appl. Surf. Sci.*, 2012, **258**, 5038-5045.
35. Y. Sun, C. J. Murphy, K. R. Reyes-Gil, E. A. Reyes-Garcia, J. M. Thornton, N. A. Morris and D. Raftery, *Int. J. Hydrogen Energy*, 2009, **34**, 8476-8484.
36. X. Y. Wang, L. X. Pang, X. Y. Hu and N. F. Han, *J. Environ. Sci.*, 2015, **35**, 76-82.
37. V. Stengl, S. Bakardjieva and N. Murafa, *Mater. Chem. Phys.*, 2009, **114**, 217-226.
38. X. Z. Li, F. B. Li, C. L. Yang and W. K. Ge, *J. Photoch. Photobio., A*, 2001, **141**, 209-217.
39. L. Zhang, Y. Man and Y. Zhu, *ACS Catalysis*, 2011, **1**, 841-848.
40. K. Y. Song, M. K. Park, Y. T. Kwon, H. W. Lee, W. J. Chung and W. I. Lee, *Chem. Mater.*, 2001, **13**, 2349-2355.
41. L. Zhou, J. Zhu, M. H. Yu, X. D. Huang, Z. Li, Y. H. Wang and C. Z. Yu, *J. Phys. Chem. C*, 2010, **114**, 20947-20954.
42. S. Adhikari and D. Sarkar, *Rsc Adv*, 2014, **4**, 20145-20153.
43. Y. P. He, Z. Y. Wu, L. M. Fu, C. R. Li, Y. M. Miao, L. Cao, H. M. Fan and B. S. Zou, *Chem. Mater.*, 2003, **15**, 4039-4045.
44. I. Aslam, C. B. Cao, M. Tanveer, M. H. Farooq, W. S. Khan, M. Tahir, F. Idrees and S. Khalid, *Rsc Adv.*, 2015, **5**, 6019-6026.
45. X. P. Lin, J. C. Xing, W. D. Wang, Z. C. Shan, F. F. Xu and F. Q. Huang, *J. Phys. Chem. C*, 2007, **111**, 18288-18293.
46. J. Jin, J. G. Yu, D. P. Guo, C. Cui and W. K. Ho, *Small*, 2015, DOI: 10.1002/smll.201500926.
47. L. S. Zhang, K. H. Wong, H. Y. Yip, C. Hu, J. C. Yu, C. Y. Chan and P. K. Wong, *Environ. Sci. Technol.*, 2010, **44**, 1392-1398.
48. Y. Chen, S. Yang, K. Wang and L. Lou, *J. Photochem. Photobiol., A*, 2005, **172**, 47-54.
49. S. Q. Liu, N. Zhang, Z. R. Tang and Y. J. Xu, *Acs Appl. Mater. Interface*, 2012, **4**, 6378-6385.
50. S. C. Yan, Z. S. Li and Z. G. Zou, *Langmuir*, 2010, **26**, 3894-3901.
51. L. Q. Ye, J. Y. Liu, C. Q. Gong, L. H. Tian, T. Y. Peng and L. Zan, *Acs Catal.*, 2012, **2**, 1677-1683.
52. A. Martinez-de la Cruz and U. M. G. Perez, *Mater. Res. Bull.* , 2010, **45**, 135-141.

RSC Advances Accepted Manuscript

53. Y. K. Du, Y. Q. Gan, P. Yang, F. Zhao, N. P. Hua and L. Jiang, *Thin Solid Films*, 2005, **491**, 133-136.
54. W. Y. Choi, A. Termin and M. R. Hoffmann, *J. Phys. Chem.*, 1994, **98**, 13669-13679.